Revision 2

Vaterite in a decrepitated diamond-bearing inclusion in zircon from a stromatic migmatite in the Chinese Sulu ultrahigh-pressure metamorphic belt

CHENHUI FEI[1, 2, 3] AND JINGBO LIU[1, 2, 3, *]

[1]*State Key Laboratory of Lithospheric Evolution, Institute of Geology and Geophysics, Chinese Academy of Sciences, Beijing 100029, China*

[2]*Innovation Academy for Earth Science, Chinese Academy of Sciences, Beijing, China*

[3]*University of Chinese Academy of Sciences, Beijing 100049, China*

*E-mail address: jingboliu@mail.iggcas.ac.cn

ABSTRACT

Vaterite was identified in a decrepitated carbonaceous material (CM)-bearing inclusion in zircon from a stromatic migmatite in the Chinese Sulu ultrahigh-pressure (UHP) metamorphic terrane. It is associated with nanometer to micrometer anhedral diamonds, aragonite, calcite, amorphous C-Si-O and amorphous Zr-Si-O materials. The inclusion developed offshoots and abundant indigenous holes. The C-Si-O material is carbon-rich and porous, and shows diagnostic Raman bands of highly disordered CM, whereas the Zr-Si-O material is spherulitic or banded with a little or no carbon. The observations from focused ion beam-scanning electron microscope (FIB-SEM) and transmission electron microscope (TEM) verify that both diamond and highly disordered

CM are of indigenous origin. The formation pathway of vaterite means that amorphous calcium carbonate (ACC) phase occurred as the precursor of vaterite. The highly disordered CM contains the subsidiary bands at 1150 and 1250 cm^{-1} on the low-frequency side of the D1 band, suggesting that there exist aliphatic hydrocarbon chains. Thus, the highly disordered CM was derived from carbonization of some kind of organic species in the fluid inclusion. Decrepitation of inclusion resulted in extremely high supersaturation rate of fluid that induced the precipitation of amorphous materials, and released relict fluid out of the inclusion, which developed a dry condition for the preservation of vaterite and amorphous materials.

Keywords: Ultrahigh-pressure metamorphism, vaterite, diamond, fluid inclusion, migmatite, Dabie-Sulu orogenic belt

INTRODUCTION

Vaterite, as one of the three polymorphs of $CaCO_3$ (vaterite, calcite and aragonite), is a rare mineral in natural rocks, but biogenic vaterite is remarkably widespread, occurring in human calculi (Rodgers 1983), pearls (Wehrmeister et al. 2009), fish otoliths (Veinott et al. 2009) and so on. In the metamorphic setting, it was reported in a contact metamorphic aureole in Ireland (McConnell 1960; Bentor et al. 1963). In the laboratory, the mixing of calcium chloride and sodium carbonate salt solutions induces supersaturation for $CaCO_3$ in solutions, leading to the precipitation of ACC phase and subsequent crystallization of vaterite at the expanse of ACC (e.g., Turnbull 1973; Ogino et al. 1987; Andreassen 2005). Vaterite is thermodynamically stable with respect to ACC, but metastable with respect to aragonite and calcite, formed at the expense of ACC due to the smaller energy barrier of vaterite nucleation than those of calcite or aragonite nucleation (De Yoreo et al. 2015). When in contact with fluid, vaterite quickly transforms to calcite or aragonite by dissolution-reprecipitation mechanism (Ogino et al. 1987; Rodriguez-Blanco et al. 2011). However, if kept dry, vaterite can be stable at up to 400 °C as a metastable mineral (Turnbull 1973).

Calcium carbonate minerals are key materials for the global carbon cycle since they can be transported to deep mantle along subduction zones. During this process, carbonic fluids were formed via metamorphic devolatilization reactions (Kerrick and Connolly, 2001) and the dissolution of carbonate minerals in fluids (e.g., Frezzotti et al. 2011; Ague and Nicolescu 2014). These fluids were recorded as fluid inclusions in minerals. Fluid

inclusions after entrapment suffered different pressure processes from those of host minerals due to the internal overpressures in fluid inclusions (e.g., Stöckhert et al. 2009; Frezzotti and Ferrando 2015). Decrepitation of fluid inclusion is a common post-trapping process along the exhumation *P-T* path of host rock when host mineral is no more able to accommodate pressure difference in and out of the inclusion. Decrepitation of fluid inclusion is a rapid process, which can result in the instantaneous precipitation of amorphous materials. Therefore, it is expectable that vaterite can be formed in decrepitated carbonate-dissolved fluid inclusions.

Here we report on a new occurrence of vaterite, which occurs in a decrepitated diamond-bearing inclusion in zircon from a stromatic migmatite in the Sulu UHP metamorphic terrane. So far, diamond is not found in this UHP metamorphic terrane, thus its identification no doubt provides a new constraint for subduction depth of the Sulu UHP rocks. The paper presents the observations of the inclusions from Raman spectroscopy, FIB-SEM and TEM, and discusses the related petrologic and geologic problems of interests.

GEOLOGICAL SETTING AND PETROGRAPHY

The Sulu UHP metamorphic terrane is the eastern extension of the Qinling–Dabie orogenic belt between the Sino–Korean Craton and the Yangtze Craton (Fig. 1a). The study is from the Weihai region, which predominantly consists of stromatic migmatites with subordinate amounts of retrograde eclogite, ultramafic rock, marble and quartzite

(Wallis et al. 2005; Liu et al. 2010; Xu et al. 2013; Li et al. 2016). Most of those lithologies record post-UHP amphibolite and granulite facies metamorphism. The UHP metamorphism of this region has been verified by coesite as inclusions in garnet from eclogites (Wang et al. 1993; Zhang et al. 1995; Nakamura and Hirajima 2000) and zircon from gneisses (Liu et al. 2010; Li et al. 2016). The eclogites display three stages of metamorphism, including UHP metamorphism, retrograde granulite facies and amphibolite facies metamorphism. The *P-T* conditions were estimated to be >2.8 GPa and 660-860 °C for UHP metamorphic stage, 0.7-1.2 GPa and 700-850 °C for granulite facies stage, and <8 kbar and 480-650 °C for amphibolite facies stage (Wang et al. 1993; Zhang et al. 1995; Nakamura and Hirajima 2000).

The investigated area consists of stromatic migmatites, pegmatites and numerous retrograde eclogite lenses. Stromatic migmatites can be divided into granitic migmatite (<5 vol.% biotite), biotite-bearing migmatite (5 vol.%), biotite-rich migmatite (5-10 vol.%) and biotite-amphibole migmatite on the basis of the volume contents of amphibole and biotite in their mesosomes. Biotite-rich migmatite is associated with biotite-amphibole migmatite as interlayers (Fig. 1b). Leucosomes with coarser-grained minerals are less than 5 cm in thickness and account for 5-30 vol.% in migmatites. They were strongly folded and foliated with the amphibolite facies mineral assemblages. Strongly foliated pegmatites as lenses and dikes are abundant in the migmatites. Retrograde eclogite bodies occur in migmatites with different sizes from several meters to ten centimeters (Fig. 1b). The sample studied (12WH-15) is from a biotite-amphibole

107 migmatite. The mesosomes are made up of plagioclase (~35 vol.%), quartz (~30 vol.%),
108 biotite (~15 vol.%), amphibole (~10 vol.%), K-feldspar (~5 vol.%), epidote (~2 vol.%)
109 and minor titanite, chlorite and Fe-oxides (Fig. 1c). Amphiboles and biotites are aligned
110 to define a schistosity. Leucosomes are less than 10 vol.%, and composed of plagioclase
111 + K-feldspar (~60 vol.%), quartz (~30 vol.%), amphibole + biotite + epidote (~5 vol.%),
112 and accessory minerals such as zircon and apatite (Fig. 1c). The modal ratios of
113 plagioclase to K-feldspar are largely variable in different leucosomes.
114

115 **SAMPLE PREPARATION AND ANALYTICAL TECHNIQUES**

116 Zircon grains were separated from the sample by standard magnetic and heavy liquid
117 techniques. Zircon separates with abundant inclusions were carefully handpicked and
118 mounted in epoxy, and then polished to approximately half of their thickness by using
119 diamond polishing paste with an average grain size of 1 μm.

120 Raman spectra were acquired using WITec confocal Raman microscope alpha 300R
121 with a 532 nm excitation laser and a thermoelectrically cooled CCD detector at Institute
122 of Geology and Geophysics, Chinese Academy of Sciences (IGGCAS). The focal spot of
123 the laser beam was 0.4 μm in diameter with a depth resolution of 0.8 μm. Analyses were
124 performed at 2-10 mW laser power with a 100× objective (numerical aperture = 0.90) at
125 300 and 1800 grooves/mm gratings. An Ar-Hg lamp was used to determine spectral
126 resolution. Gaussian fitting of the 577 nm emission line yielded full width at half
127 maximum (FWHM) values of about 8.9 and 0.9 cm^{-1} at the two gratings, respectively.

128 The 300 grooves/mm grating was mainly used to map the inclusions because it allowed to
129 obtain a spectrum from 100 to 4000 cm^{-1} in a spectral window. The 1800 grooves/mm
130 grating was used to obtain the spectra with higher spectral resolution, which can better
131 distinguish the triplet of vaterite in the region between 1075 and 1090 cm^{-1} (Wehrmeister
132 et al. 2009). For a selected area (usually rectangle), Raman mapping was generated at the
133 step of 0.3-0.5 μm with an acquisition time of 3-5 seconds and one accumulation. The
134 band parameters of diamond and highly disordered CM, including FWHM, position, area
135 and amplitude, are obtained by band fitting. A linear baseline was fitted to spectra for
136 background correction. Band shape is defined by a Gaussian/Lorentzian hybrid function.
137 Band fitting was carried out using Peakfit v4.12 software. FWHM was corrected using
138 measured FWHM and the instrumental profile function about 8.9 cm^{-1} width at the 300
139 grooves/mm grating and 0.9 cm^{-1} width at the 1800 grooves/mm grating (Váczi 2014;
140 Nasdala et al., 2016). In the region of 1000-1800 cm^{-1}, the Raman spectrum of CM
141 contains two main bands, i.e., the disordered (D1) band at about 1350 cm^{-1} and the
142 graphite (G) band at about 1580 cm^{-1} (e.g., Beyssac et al., 2002). Some additional bands
143 often occur in highly disordered CM, including D2 at about 1620 cm^{-1}, D3 at about 1510
144 cm^{-1}, D4 at about 1250 cm^{-1}, D5 at about 1150 cm^{-1}, D6 at about 1440cm^{-1} (Ferralis et al.
145 2016; Henry et al. 2019). In our sample, a band at about 1085 cm^{-1} can also be observed.
146 At the same time, the D2 band is hardly discernible from the G band. Therefore, a band
147 of combination of G + D2, together with D1, D3, D4, D5, D6 and a band of 1085 cm^{-1}, is
148 used to deconvolute the Raman spectra of CM in the sample in the spectral range from

This is the peer-reviewed, final accepted version for American Mineralogist, published by the Mineralogical Society of America.
The published version is subject to change. Cite as Authors (Year) Title. American Mineralogist, in press.
DOI: https://doi.org/10.2138/am-2021-7940. http://www.minsocam.org/

149 1020 to 1800 cm^{-1} (The position of 1020 cm^{-1} was selected in order to avoid the
150 interference of the 1008 cm^{-1} band of zircon).

151 FIB-SEM at IGGCAS was used to observe diamond-bearing inclusions and obtain
152 foil for the observation of TEM. FIB foils were prepared using a Zeiss Auriga Compact
153 dual beam system with a Ga-ion beam. The conditions for milling were 5-30 kV voltage
154 with a beam current of 12-500 pA. Secondary electron (SE) images were acquired at
155 1.5-10 kV accelerating voltage. There is not any coating to be applied to foil. Two foils
156 were prepared: one with about 10×10 μm^2 area was milled to about 0.8 μm thickness for
157 Raman analysis, and further cut to about 100 nm thickness for TEM observation; the
158 other was milled to about 100 nm thickness and 6×6 μm^2 area for TEM observation.

159 The FIB-prepared foils of inclusions were observed using a JEOL JEM-2100 TEM
160 with energy-dispersive X-ray spectrometer (EDS) at a 200 kV at IGGCAS. The
161 illumination area for electron diffractions is about 130 nm, and selected area electron
162 diffraction (SAED) image is taken at a camera length of 30 cm. Some nanometer crystals
163 were observed using high-resolution TEM (HRTEM) image, and their fast Fourier
164 transform (FFT) diffraction patterns were obtained from the HRTEM images. The
165 comparison between the measured d-spacings and interplanar angles of the diamonds in
166 the sample and the calculated corresponding d-spacings and interplanar angles of the
167 diamond from American Mineralogist Crystal Structure Database (Downs and
168 Hall-Wallace 2003) shows that the relative error is < 3% for the measured d-spacings,
169 and the error is < 2° for the measured interplanar angles (Tables S2 and S3). EDS analysis

and X-ray compositional mapping were performed at 200 kV with a beam current of 106 μA and a beam size of 10 nm using Oxford Aztec software.

RESULTS

The zircon studied is an isometric grain with a diameter of about 70 μm (Fig. 2a-d). Four zones are identified based on cathodoluminescence (CL) image (Fig. 2a). Zone I is predominant with complicated patches of different CL emissions. Previous relict zircon can still be identified in Zone I. The other three zones (II-IV) are discrete thin layers with different CL emissions. The inclusions are concentrated in Zone I (Fig. 2), which were intensively studied using Raman spectroscopy, FIB-SEM and TEM.

Raman observations

Raman maps of inclusions in zircon are displayed in Fig. 2e-m. Several types of inclusions were identified, including CM-bearing inclusions, CO_2 fluid inclusions, melt inclusions, oxide and sulphate solid inclusions. The Raman-based identification of minerals may refer to the RRUFF online database (https://rruff.info/) (Lafuente et al. 2015).

CM-bearing inclusions are characterized by diamond and highly disordered CM. Identified assemblages in three inclusions are Vtr + Dia + Cal in inclusion 4, Dia + Ant + highly disordered CM in inclusion 5, and Rt + highly disordered CM + Zrn in inclusion 9 (mineral abbreviations in the figure caption of Figs. 1 and 2; Fig. 2e-g). The diagnostic Raman bands are shown in Fig. 3 and Supplementary Fig. S1. Vaterite is identified in

191 inclusion 4 by bands 1090, 1081, 1075, 752, 301, 267, 176, 150, 121, 105 cm^{-1} (Fig. 3a
192 and b; Behrens et al. 1995; Anderson 1996; Wehrmeister et al. 2009). Calcite contains the
193 bands 1086, 712, 281 and 153 cm^{-1} (Fig. 3b), however TEM observation shows that
194 aragonite was also present in the inclusion (see TEM observations). Diamond shows the
195 band at 1330-1333 cm^{-1} (Fig. 3a-c). The highly disordered CM is characteristic of the D1
196 band at 1350-1380 cm^{-1} and the G band at 1560-1580 cm^{-1} with broad FWHM, indicating
197 that it is highly disordered sp^2-bonding graphic carbon (Fig. 3d). Other minerals
198 identified include zircon (Fig.2g, Zrn 1; Fig. S1b), anatase (Fig. 2f and Fig. S1c), and
199 rutile (Fig.2g and Fig. S1d). The 356 cm^{-1} band displays a striking difference in intensity
200 between Zrn 1 and the host zircon, reflecting the difference in lattice orientations of the
201 two zircons (Fig. S1a and b).

202 The CO_2 fluid inclusions less than 3 μm in size (Fig. 2d and h, inclusions 11 and 12),
203 display the diagnostic bands at 1282 and 1386 cm^{-1} (Fig. 3e) (e.g., Rosso and Bodnar,
204 1995).

205 Melt inclusions are abundant in the zircon (Fig. 2f, i-k and m). The observed
206 assemblages include Ab + Qz (inclusion 2), Kml + Kok + Cal + Ms + Glass (inclusion 6),
207 Kok + Cal + Kml (inclusion 8), Kfs + Ms (inclusion 13), and Qz + Kok + Kml (inclusion
208 14). Kokchetavite was identified by the Raman bands at 391, 108 and 833 cm^{-1} (Fig. S1e
209 and f) (Kanzaki et al. 2012), and kumdykolite by the Raman bands at 491 and 155 cm^{-1}
210 (Fig. S1f) (Hwang et al. 2009). The granitic glass, which can be directly observed in melt
211 inclusions exposed in polishing surfaces of zircons (Supplementary Fig. S2), is

212 characterized by a prominent broad Raman band from about 300 to 550 cm^{-1} centered at
213 470-490 cm^{-1} (Figs. S1e and f and S2), similar to those reported by Cesare (2009) and
214 Ferrero et al. (2016). The Raman spectra of other minerals, including K-feldspar, albite,
215 quartz and muscovite, were given in Fig. S1g-j.

216 Oxide solid inclusions include hematite and rutile (Fig. 2f, h, k and m). Hematite is
217 very small (<2 μm), displaying the bands at 1318, 610, 411, 292 and 226 cm^{-1} (Fig. S1k).
218 Rutile is relatively large in size (Fig. 2m), with the bands at 612, 445, 239 and 144 cm^{-1}.
219 A sulphate solid inclusion consists of anhydrite and barite (Fig. 2l, inclusions 10), whose
220 Raman spectra are shown in Fig. S1l.

221

222 **FIB-SEM observations**

223 Two diamond-bearing inclusions (4 and 5) have been exposed in polishing surface. In
224 order to determine the origin of diamond, FIB-SEM is used to observe the two inclusions.
225 Two trenches were dug along both sides of an inclusion (Figs. 4a and 5a). The inclusions
226 in the vertical cross-sections of trenches were observed using SE and X-ray
227 compositional images.

228 Figure 4 shows SE images and X-ray compositional images of the vertical
229 cross-sections of inclusion 4. On the top of the inclusion, several coating layers can be
230 observed (Fig. 4b), including a protective Pt-C coating, a Pt coating, and two relict Au
231 coatings from top to bottom. Au coating had been applied twice to the sample before FIB
232 milling, which were cleaned but some Au relicts are still remained on the top of the

233 inclusion. For FIB milling, a Pt coating was first applied to the sample, and then an
234 additional protective Pt-C coating was sprayed on the top of the inclusion to protect them
235 from milling destruction. A little of debris can be observed in those coatings. The top
236 surface of the inclusion is a concave-upward rough surface that formed during polishing
237 process. The inclusion consists of large holes, porous material, spherulitic aggregate as
238 well as mineral grains (Fig. 4a-c). X-ray compositional images reveal that the inclusion
239 includes pure carbon areas, carbon-rich spots, Ca-rich area, C-Si-O and Zr-Si-O areas
240 (Fig. 4d-h). According to the results from Raman mapping, the pure carbon areas and
241 carbon-rich spots correspond to diamond grains, and the Ca-rich area to carbonate
242 minerals. The C-Si-O and Zr-Si-O areas correspond to the porous material and spherulitic
243 aggregate, respectively. However, carbon is identified in these materials on the basis of
244 X-ray compositional analysis (Fig. 4d). It is evident that diamonds are enclosed in the
245 porous material and spherulitic aggregate (Fig. 4b-d). In addition, an offshoot is present at
246 the lower right corner of the inclusion (Fig. 4a and b).

247 Representative SE images of inclusion 5 were displayed in Fig. 5. The pit on the top
248 of the inclusion is 1-1.5 μm depth, and contains relict coating Au and more debris
249 forming in polishing and cleaning process (Fig. 5a and b). The inclusion with some large
250 holes shows a feature of necking-down (Fig. 5a and b). A spherulite enclosed in banded
251 material occurs in the upper part (Fig. 5b), while the lower part consists of five carbon
252 grains, banded material and porous material (Fig. 5b and c). X-ray compositional images
253 show that the spherulite contains Ti, Ca, Si with Al and Fe (Fig. 5e-h), in which anatase

254 was identified on the basis of Raman mapping. The banded material around the spherulite
255 consists of Zr, Si and O (Fig. 5f-h). In the lower part, five carbon grains correspond to
256 diamond, and the banded material and porous material to Zr-Si-O and C-Si-O materials,
257 respectively. Diamonds are enclosed in the banded and porous materials (Fig. 5b, and
258 Supplementary Fig. S3). Offshoots were well developed at some corners of the inclusion
259 (Fig. 5a and b).

260 Raman mapping shows that the foil taken from inclusion 5 contains diamond, highly
261 disordered CM and anatase (Fig. 6). The band position of diamond ranges from 1321 to
262 1326 cm^{-1} with the FWHM of 3.0-5.0 cm^{-1}, displaying an evident downshift in
263 comparison with the results measured before FIB milling (Fig. 6d), which should be a
264 result of structural damage of diamond caused by the impingement of high energy
265 Ga-beam in the process of FIB milling (Nasdala et al., 2013, 2016). Highly disordered
266 CM occurs in the porous and banded materials. The D1 and G bands at different sites
267 display variations in band-position and band-intensity (Fig. 6e). Band-fitting results
268 shows that the shoulder on the low-frequency side of the D1 band consists of three
269 subsidiary bands 1082-1095 cm^{-1}, 1138-1147 cm^{-1} (D4), 1227-1260 cm^{-1} (D5) (Fig. 6e;
270 Supplementary Table S1). The breathing vibration of aromatic ring (D1) ranges from
271 1338-1372 cm^{-1} with the FWHM of 140-192 cm^{-1}, the G + D2 is located between 1566
272 and 1582 cm^{-1} with the FWHM of 95-129 cm^{-1}, and the bands D3 and D6 are in
273 1463-1510 cm^{-1} and 1388-1438 cm^{-1}, respectively (Table S1).

274

TEM observations

TEM observations on inclusion 4, including bright field (BF) image, HRTEM image, SAED pattern, and EDS analysis, are shown in Figs. 7 and 8. The d-spacings of diamond, vaterite and aragonite measured from SAED patterns were listed in Supplementary Table S2.

Two of three carbonate mineral grains are vaterite in the foil (Fig. 7). Their compositions consist of Ca, C and O (Fig. 8a). The large platy vaterite has an orthorhombic crystal structure with space group *Pbnm* (Fig. 8b; Table S2), whereas the small one shows a hexagonal crystal structure with space group $P6_3/mmc$ (Table S2). Another small carbonate mineral is aragonite (Fig. 8c; Table S2). This grain of aragonite was not identified by Raman analysis due to too small size.

Diamonds show two groups in size: micrometer group with 0.4-1 μm (Fig. 7a) and nanometer group with less than 100 nm (Fig. 7b-d; Table S2). EDS analyses show pure carbon for micrometer diamonds (Fig. 8d), whereas nanometer diamond contains minor Si, Zr and O from host materials (Fig. 8g). The diamonds were further verified by their SAED patterns. The zone-axis patterns, measured d-spacings and angles between zone axis patterns are all consistent with diamond unit cell (Fig. 8e, f, h and i; Table S2). EDS analyses and SAED patterns show that porous material is carbon-rich amorphous C-Si-O material (Fig 8j and l), whereas spherulitic material is amorphous Zr-Si-O material with a little or no carbon (Fig 8k and m). Two kinds of amorphous materials plot in different compositional areas in the Zr-C-Si triangle diagram according to semi-quantitative EDS

296 analytical results (Fig. 9).

297 BF and HRTEM images show that nanometer diamonds are enclosed in the
298 amorphous materials (Fig. 7b-e), and the interface between diamond and amorphous
299 material is fully coupled and welded boundary (Fig. 7d and e). At the same time, the
300 interface between micrometer diamond and amorphous material also shows the same
301 contact (Supplementary Fig. S4).

302 TEM observations of inclusion 5 were shown in Fig. 10 and Supplementary Fig. S5
303 and Table S3. Five carbon grains are all consistent with diamond (Fig 10c and d; Table
304 S3). EDS analyses show that the banded material is made up of Zr, Si and O with a little
305 or no carbon, and SAED patterns and HRTEM images show that the Zr-Si-O material
306 consists of nanocrystals plus amorphous material in some domains (nc-Zr-Si-O; Fig. 10e
307 and f ; Fig. S5), but complete amorphous material in other domains (a-Zr-Si-O; Fig. 10g
308 and h). Four FFT diffraction patterns from nanocrystals correspond to elpidite crystal
309 structure (Fig. S5; Table S3). However, the reason for Na not detected in EDS analysis is
310 probably due to electron-beam-induced vaporization of Na since EDS analysis was
311 performed with a very high voltage (200 kV) and a very small beam size (10 nm). The
312 banded texture in the Zr-Si-O material, shown in SE and BF images (Fig. 5b and c; Fig.
313 10a), is compositional banding induced by the fluctuation of Zr and Si contents. The dark
314 layers in BF image are rich in Zr and poor in Si (Fig. 10b). The porous material, mainly
315 consisting of C, Si and O with minor other elements such as Ca and Zr, is amorphous
316 material (Fig. 10i and j). There exists a compositional gap between Zr-Si-O and C-Si-O

317 materials (Fig. 9).

318 The spherulite in the upper part of inclusion 5 consists of nanometer minerals and
319 amorphous material (Fig. 5b; Supplementary Fig. S6a). Besides anatase determined from
320 Raman analysis, vesuvianite, perovskite and xonotlite were also identified (Fig. S6b-g;
321 Table S3). Four SAED patterns obtained from two grains, which mainly consist of Ca, Si,
322 and O with moderate Al, Fe and Mg similar to vesuvianite in compositions (Fig. S6b), are
323 consistent with vesuvianite crystal structure (Fig. S6c; Table S3). Four grains composed
324 of Ca, Ti and O (Fig. S6d) show the SAED patterns of perovskite with two space groups
325 *Pbnm* and *Pm-3m*, respectively (Fig. S6e; Table S3). Semi-quantitative EDS analysis
326 shows that the mineral consisting of Ca, Si and O has an atomic number ratio 1:0.8:2.8
327 (Fig. S6f), closest to the ratios of xonotlite (1:1:3.2) and wollastonite (1:1:3). However,
328 the SAED pattern fits for xonotlite rather than wollastonite (Fig. S6g; Table S3).

329

330 ## DISCUSSIONS

331 ### Diamond origin

332 Two diamond-bearing inclusions were exposed in polishing surface, leading to a
333 reasonable suspicion that diamonds are from diamond paste in sample preparation. A
334 contaminated inclusion is characteristic of mechanical mixing deposition, which diamond
335 fragments from diamond paste mixed with epoxy resin and debris from polishing process
336 were deposited in inclusion (Dobrzhinetskaya et al., 2014). Therefore, as suggested by
337 Nasdala et al. (2016), the inclusions exposed in polishing surface need additional

techniques such as TEM analysis of FIB-prepared foils to verify the origin of diamond. For the inclusions studied, the most key question is how to interpret the origin of the C-Si-O and Zr-Si-O materials since diamonds are enclosed in those materials, and the interface between diamond and amorphous material is fully coupled and welded boundary. Several crucial lines of evidence support indigenous origin of diamond and highly disordered CM, including (1) the C-Si-O and Zr-Si-O materials as well as vaterite and aragonite in our sample, are natural materials. Epoxy resin used in our sample preparation consists of C-O-H-Cl (Supplementary Fig S7a), and is totally different from the C-Si-O and Zr-Si-O materials in compositions (Figs. 5, 8, 9 and 10); (2) the highly disordered CM in our sample is characteristic of the D1 and G modes, whereas epoxy resin is a kind of organic matter that has different Raman vibrations and does not contain any highly disordered CM (Fig S7b). Our experiment shows that the impingement of high energy Ga-beam in the process of FIB milling can completely destroy the chemical bonds of epoxy resin, producing new amorphous carbonaceous matter that the Raman bands of epoxy resin completely disappear. However, the new amorphous carbonaceous matter has only a weak G band (Fig S7c and d). The lack of the D1 band suggests that there does not exist aromatic carbon cluster in such amorphized epoxy resin. In contrast, the highly disordered CM in our sample developed the D1 band, and thus contains aromatic carbon clusters (Fig S7c-e). The formation of aromatic carbon clusters in highly disordered CM needs high temperature conditions (Beyssac et al. 2002; Table S1), which was not reached in the process of sample preparation. Therefore, epoxy resin is not present in

359 inclusions 4 and 5. In addition, the vertical cross-section of foil of epoxy resin is very
360 smooth and flat (Fig S7d), similar to the case of milled minerals, and any hole or pit was
361 not observed on the vertical cross-section of the foil, reflecting epoxy resin cannot be
362 "evaporated" during the process of FIB milling; (3) the two inclusions display natural
363 spherulitic and banded textures (Figs. 4, 5, 6 and 10 and Fig. S5). Mechanical mixing
364 deposition does not form such textures. The spherulitic texture typically occurs in
365 precipitates from supersaturated fluids (De Yoreo et al. 2015), whereas the banded texture
366 reflects periodic precipitation of material in fluids (Frezzotti and Ferrando 2015). The
367 compositional banding in the Zr-Si-O material is parallel to the boundaries of diamonds
368 (Figs. 6a and 10a), reflecting a periodic growth of the Zr-Si-O material around diamonds.
369 The Zr-Si-O material is rigid solid materials rather than soft viscous material. If exotic
370 diamonds squeezed into the material, the banded texture would be destroyed. However,
371 we do not observe any fracture in the banded Zr-Si-O material (Figs. 6a and 10a), and the
372 compositional banding around diamonds are completely preserved. Therefore, these
373 observations can rule out that the diamonds enclosed in the banded Zr-Si-O material are
374 exotic. The complete preservation of compositional banding also indicates that nanometer
375 elpidites in the compositional banding (Fig. S5) were crystallized from the amorphous
376 materials rather than mechanical debris from polishing process; (4) the diamonds are
377 enclosed inside the C-Si-O and Zr-Si-O materials (Figs. 6 and 7). Especially, nanometer
378 diamonds in inclusion 4 are enclosed inside the C-Si-O and Zr-Si-O materials, and
379 HRTEM images show that the interface between diamond and host amorphous materials

is fully coupled and welded (Figs. 6a, 7 and Fig. S4). Therefore, these observations support that the diamonds in our sample are indigenous.

In addition, the micrometer diamonds in the inclusions are mostly elongate grains with irregular to flat boundaries (Supplementary Fig. S8a), whereas the diamonds in polishing paste are irregular equant grains (Fig. S8b), which their ratios of the major and minor axes show a systematical difference (Fig. S8c). Nanometer diamond with <100 nm was not observed in polishing paste. There were two possible processes to control morphological feature of the diamonds in the inclusions. The diamonds possibly suffered a decomposition in the exhumation process of the host rock, which their rims were reacted or absorbed, and decrepitation of inclusion possibly resulted in diamond fracturing.

Amorphous materials

Observed amorphous materials include the C-Si-O and Zr-Si-O materials. Vaterite suggests the presence of ACC phase as the precursor of vaterite. Therefore, inclusion 4 contains three kinds of amorphous materials, whereas inclusion 5 only contains amorphous C-Si-O and Zr-Si-O materials. The C-Si-O material is porous, whereas the Zr-Si-O material show as spherulitic in inclusion 4 and as banded in inclusion 5. The two inclusions developed large holes and offshoots that were filled by the amorphous materials (Figs. 4 and 5). All the phenomena observed suggest that the inclusions are decrepitated fluid inclusions, where amorphous materials were precipitated in the

401 decrepitation process of fluid inclusions, and the holes are derived from the escape of
402 fluid.

403 The precipitates provide crucial information for fluid compositions and nature. The
404 main compositions of the two inclusions may be described using the
405 $ZrSiO_4$-$CaCO_3$-SiO_2-C-H_2O-CO_2 system with minor TiO_2, FeO and Al_2O_3 as indicated by
406 Raman, FIB-SEM and TEM observations. The presence of CO_2 is indicated by CO_2 fluid
407 inclusions around large CM-bearing inclusions and melt inclusions (Fig. 2c and d). The
408 fluids manifested by inclusions 4 and 5 were impossibly equilibrated with bulk rock on
409 the judgment of their compositions, but locally equilibrated with zircon, carbonate and
410 SiO_2 minerals. The volume contents of precipitates in the two inclusions account for over
411 50 % on the basis of the observations of FIB-milling vertical cross-sections (Figs. 4 and
412 5). Such high contents of solutes are hardly explained using the solubilities of quartz (e.g.,
413 Shmulovich et al. 2001; Zotov and Keppler 2002), calcite/aragonite (Caciagli and
414 Manning 2003; Facq et al. 2014) and zircon (Ayers et al. 2012), but indicate that the
415 inclusions contain solute-rich supercritical fluids with a transitional feature between melt
416 and aqueous fluid. In addition, the C-Si-O and Zr-Si-O materials are coexisting
417 amorphous phases with a striking compositional gap (Fig. 9), reflecting an immiscibility
418 between them, which should be a result of phase separation in glass occurring in the
419 precipitation process (Vogel 1977).

420 The amorphous materials in our sample only show highly disordered CM bands,
421 suggesting that the highly disordered CM occurs as independent disordered carbon

clusters in the amorphous materials. The in-plane sizes of aromatic carbon clusters in highly disordered CM, calculated on the basis of the ratio of integrated D1 and G intensities (I_{D1}/I_G) and the excitation laser energy of 2.34 eV (532 nm) (Cancado et al. 2006), range from 11 to 22 nm. The highly disordered CM also shows a subsidiary band at about 1085 cm^{-1}, which is probably originated from carbonate material. Among the Raman bands of CM, the D4 and D5 bands are not present in highly carbonized and graphitic materials but in fairly immature organic materials or in functionalized carbon systems that are related to the CH species in aliphatic hydrocarbon chains (Schopf et al. 2005; Ferralis et al. 2016). There is a strong positive correlation between the intensity of D5 or D4 + D5 band and the atomic ratio *H:C* in the range between almost pure graphite (*H:C* = 0.01) and weak metamorphosed kerogen (*H:C* = 0.65) (Ferralis et al. 2016). The highly disordered CM in the sample gives the *H:C* ratios from 0.45 to 0.81 (Table S1). Therefore, the highly disordered CM is mainly composed of aromatic carbon clusters and aliphatics or aliphatic chains attached to the aromatic carbon clusters, indicating that it was derived from decomposition of organic matter in fluid inclusions. This result supports those organic matters such as aliphatic acids or anions are stable species (Sverjensky et al. 2014; Sverjensky and Huang 2015), and can be synthesized in eclogitic fluids (Frezzotti 2019).

The presence of organic species in the inclusions means that the fluids were reductive. However, it seems to be contradicted with the presence of highly oxidized solid inclusions of hematite and anhydrite + barite. As mentioned before, Zone I of zircon

443 contains relict inherited zircon, abundant melt and fluid inclusions, indicating that Zone I
444 was formed via dissolution-precipitation of inherited zircon. In fact, hematite, biotite and
445 apatite inclusions were often identified in inherited zircon cores in our sample. Therefore,
446 hematite and barite + anhydrite inclusions in Zone I probably are inherited.
447

448 **Precipitation of amorphous materials**

449 Amorphous materials, including ACC, C-Si-O and Zr-Si-O materials, are metastable
450 materials, precipitating from extremely supersaturated fluids. Meanwhile, low
451 temperature condition and dry setting are also key factors for the preservation of
452 amorphous materials.

453 The fluid inclusions were trapped in UHP metamorphic process with the *P-T*
454 condition of 700-900 °C and >3.5 GPa (Fig. 11). Before the precipitation of ACC, C-Si-O
455 and Zr-Si-O materials, crystalline materials in fluids only include a little number of
456 diamonds with <1 μm in inclusion 4. Vaterite can provide a constraint on the precipitation
457 temperature of the amorphous materials due to its unique formation pathway. Vaterite
458 crystallizes at the expanse of ACC phase within several minutes after ACC precipitates.
459 The precipitation occurred under the upper limit of 400 °C that vaterite can be stable. At
460 the same time, the highly disordered CM in our sample can also be used to constrain the
461 precipitation temperature by the Raman carbonaceous-material geothermometer (Beyssac
462 et al. 2002; Rahl et al. 2005). The two geothermometers give almost consistent
463 temperature estimates with the average results of 386 ± 27 °C and 409 ± 35 °C (Table S1).

In addition, other materials in inclusion 5 are the latest low-temperature phases, e.g., vesuvianite with *P4/nnc* polytype formed in a temperature range from 300 to 500 °C (Gnos and Armnruster 2006); xonotlite is stable under 450 °C, decomposing to wollastonite + H_2O at high temperature side (Pistorius 1963). Therefore, there is a temperature difference of about 400 °C between the entrapment of the inclusion and the precipitation of the amorphous materials, meaning that the fluids in inclusions were supersaturated before the precipitation of amorphous materials. Small size of fluid inclusions (<10 μm in diameter) and the presence of organic crystallization inhibitor probably play an important role for the formation of supersaturated fluids in inclusions (Putnis et al. 1995).

However, the precipitation of amorphous materials still needs a rapid process that leads to an extreme high supersaturation rate in the fluids in inclusions (cooling rate when pressure is not considered) (Putnis et al. 1995). In principle, the amount of dissolved substance in a fluid depends on temperature and pressure. Therefore, an extreme high supersaturation rate of fluid can be induced by rapid pressure change of the fluid. The decrepitation or partial decrepitation of fluid inclusion can induce huge pressure drop on a time scale of second, resulting in extreme high supersaturation rate for precipitation of amorphous phases. Therefore, the decrepitation of fluid inclusion should be responsible for the formation of the amorphous materials in the inclusion. At the same time, the decrepitation of fluid inclusion also plays a role in the preservation of amorphous phases. Relict fluid was released out of inclusion in the decrepitation process so that vaterite can

485 be preserved, otherwise vaterite would transform quickly to calcite or aragonite (Ogino et
486 al. 1987; Rodriguez-Blanco et al. 2011).
487
488 **Inclusion evolution**
489 The rocks in the Weihai region experienced a nearly isothermal decompression
490 exhumation from UHP stage to granulite facies stage, following a cooling stage (Fig. 11)
491 (Zhang et al. 1995; Nakamura and Hirajima 2000). The presence of diamond suggests
492 that the peak pressure is not lower than 3.5-4.0 GPa between 700 and 900 °C. The
493 well-developed offshoots at some corners around the two inclusions (Figs. 4 and 5),
494 verify that overpressures occurred in the inclusions in the exhumation process of host
495 rock. The offshoots were filled by the C-Si-O and Zr-Si-O materials, suggesting that the
496 precipitation immediately followed decrepitation. The banded Zr-Si-O material in
497 inclusion 5 indicates a periodically precipitating process, possibly corresponding to a
498 partial decrepitation process (e.g, Stöckhert et al. 2009; Frezzotti and Ferrando 2015),
499 whereas spherulitic precipitate in inclusion 4 suggests a complete decrepitation with
500 offshoot propagating to the surface of host zircon.
501 Together with temperature constraints from vaterite and highly disordered CM, sketch
502 *P-T* evolutions of inclusions 4 and 5 are shown in Fig. 11. The melt inclusions and fluid
503 inclusions were trapped at UHP stage. Partial melting of rocks causes drastic reduction in
504 the strength and viscosity of rocks (Rosenberg and Handy 2005), triggering the
505 exhumation of UHP terrane as isothermal diapiric rise (Wallis et al. 2005). In this process,

506 the inclusions evolved independently from the host zircon due to internal overpressure as
507 shown in Fig. 11. Inclusion 5 with larger size experienced a series of decrepitation events
508 indicated by some short offshoots (Fig. 5), whereas smaller inclusion 4 suffered a
509 complete decrepitation resulted in fluid evacuation from the inclusion.
510

511 **IMPLICATIONS**

512 Vaterite as a rare mineral was found in a diamond-bearing inclusion in zircon from a
513 stromatic migmatite in the Sulu UHP metamorphic terrane. It has a specific formation
514 pathway that crystallizes at the expense of ACC, and its preservation needs a dry
515 condition. A decrepitation process of fluid inclusion can explain the formation and
516 preservation of vaterite. Other materials associated with vaterite include diamond,
517 amorphous C-Si-O and Zr-Si-O materials. The observations from FIB-SEM and TEM
518 confirm their indigenous origin. The presence of diamond, as a first identification in the
519 Sulu UHP metamorphic terrane, can further constrain metamorphic pressure condition.
520 The highly disordered CM contains the subsidiary bands at 1150 and 1250 cm^{-1},
521 suggesting that there exist aliphatic hydrocarbon chains in the highly disordered CM.
522 Therefore, the highly disordered CM in our sample is from carbonization of organic
523 matter.

524 Other types of inclusions such as melt inclusions, CO_2 fluid inclusions, oxide and
525 sulphate solid inclusions were also identified in zircon, suggesting that the inclusions
526 were trapped at UHP conditions when host rock was partially melted. The partial melting

527 of the Weihai rocks occurred at UHP stage rather than during the exhumation process of
528 rocks, thus it triggered the exhumation of UHP terrane. The melt and fluid inclusions in
529 zircons record an immiscible melt-fluid system. Among them, carbon shows a variety of
530 species, presenting in CO_2, carbonate, diamond and amorphous carbon, which provides
531 important information for carbon speciation in the fluids of subduction zones.
532

533 **ACKNOWLEDGEMENTS**

534 We thank Gu Lixin and Tang Xu for their assistance in FIB-SEM and TEM analyses,
535 and Prof. Yang Jianjun for stimulating discussion and correcting the manuscript. This
536 study was supported by the National Natural Science Foundation of China (No. 41372080)
537 and State Key Laboratory of Lithospheric Evolution (No. 201707).
538

539 **REFERENCES CITED**

540 Ague, J.J., and Nicolescu, S. (2014) Carbon dioxide released from subduction zones by
541 fluid-mediated reactions. Nature Geoscience, 7(5), 355-360.
542 Anderson, A. (1996) Group theoretical analysis of the v_1 (CO_3^{2-}) vibration in crystalline
543 calcium carbonate. Spectroscopy Letters, 29(5), 819-825.
544 Andreassen, J.P. (2005) Formation mechanism and morphology in precipitation of
545 vaterite-nano-aggregation or crystal growth? Journal of Crystal Growth, 274(1-2),
546 256-264.
547 Ayers, J.C., Zhang, L., Luo, Y., and Peters, T.J. (2012) Zircon solubility in alkaline

548 aqueous fluids at upper crustal conditions. Geochimica et Cosmochimica Acta, 96,
549 18-28.
550 Behrens, G., Kuhn, L.T., Ubic, R., and Heuer, A.H. (1995) Raman spectra of vateritic
551 calcium carbonate. Spectroscopy Letters, 28(6), 983-995.
552 Bentor, Y., Gross, S., and Heller, L. (1963) Some unusual minerals from the "Mottled
553 Zone" complex, Israel. American Mineralogist: Journal of Earth and Planetary
554 Materials, 48(7-8), 924-930.
555 Beyssac, O., Goffe, B., Chopin, C., and Rouzaud, J.N. (2002) Raman spectra of
556 carbonaceous material in metasediments: a new geothermometer. Journal of
557 Metamorphic Geology, 20(9), 859-871.
558 Caciagli, N.C., and Manning, C.E. (2003) The solubility of calcite in water at 6-16 kbar
559 and 500-800 °C. Contributions to Mineralogy and Petrology, 146(3), 275-285.
560 Cancado, L.G., Takai, K., Enoki, T., Endo, M., Kim, Y.A., Mizusaki, H., Jorio, A., Coelho,
561 L.N., Magalhaes-Paniago, R., and Pimenta, M.A. (2006) General equation for the
562 determination of the crystallite size L-a of nanographite by Raman spectroscopy.
563 Applied Physics Letters, 88, 163106. https://doi.org/10.1063/1.2196057.
564 Cesare, B., Ferrero, S., Salvioli-Mariani, E., Pedron, D., & Cavallo, A. (2009).
565 "Nanogranite" and glassy inclusions: The anatectic melt in migmatites and
566 granulites. Geology, 37(7), 627-630. https://doi.org/10.1130/G25759A.1
567 De Yoreo, J.J., Gilbert, P.U., Sommerdijk, N.A., Penn, R.L., Whitelam, S., Joester, D.,
568 Zhang, H., Rimer, J.D., Navrotsky, A., Banfield, J.F., Wallace, A.F., Michel, F.M.,

569 Meldrum, F.C., Colfen, H., and Dove, P.M. (2015) Crystallization by particle
570 attachment in synthetic, biogenic, and geologic environments. Science, 349(6247),
571 aaa6760.
572 Dobrzhinetskaya, L., Wirth, R., and Green, H. (2014) Diamonds in Earth's oldest zircons
573 from Jack Hills conglomerate, Australia, are contamination. Earth and Planetary
574 Science Letters, 387, 212-218.
575 Downs, R.T., and Hall-Wallace, M. (2003) The American Mineralogist Crystal Structure
576 Database. American Mineralogist, 88, 247-250.
577 Facq, S., Daniel, I., Montagnac, G., Cardon, H., and Sverjensky, D.A. (2014) In situ
578 Raman study and thermodynamic model of aqueous carbonate speciation in
579 equilibrium with aragonite under subduction zone conditions. Geochimica et
580 Cosmochimica Acta, 132, 375-390.
581 Ferralis, N., Matys, E.D., Knoll, A.H., Hallmann, C., and Summons, R.E. (2016) Rapid,
582 direct and non-destructive assessment of fossil organic matter via microRaman
583 spectroscopy. Carbon, 108, 440-449.
584 Ferrero, S., Ziemann, M.A., Angel, R.J., O'Brien, P.J., and Wunder, B. (2016)
585 Kumdykolite, kokchetavite, and cristobalite crystallized in nanogranites from felsic
586 granulites, Orlica-Snieznik Dome (Bohemian Massif): not evidence for
587 ultrahigh-pressure conditions. Contributions to Mineralogy and Petrology, 171(1), 3.
588 Frezzotti, M.L. (2019) Diamond growth from organic compounds in hydrous fluids deep
589 within the Earth. Nature Communications, 10(1), 4952.

590 Frezzotti, M.L., and Ferrando, S. (2015) The chemical behavior of fluids released during
591 deep subduction based on fluid inclusions. American Mineralogist, 100(2-3),
592 352-377.
593 Frezzotti, M.L., Selverstone, J., Sharp, Z.D., and Compagnoni, R. (2011) Carbonate
594 dissolution during subduction revealed by diamond-bearing rocks from the Alps.
595 Nature Geoscience, 4(10), 703-706.
596 Gnos, E., and Armbruster, T. (2006) Relationship among metamorphic grade, vesuvianite
597 "rod polytypism," and vesuvianite composition. American Mineralogist, 91(5-6),
598 862-870.
599 Henry, D.G., Jarvis, I., Gillmore, G., and Stephenson, M. (2019) Raman spectroscopy as
600 a tool to determine the thermal maturity of organic matter: Application to
601 sedimentary, metamorphic and structural geology. Earth-Science Reviews, 198,
602 102936. https://doi.org/10.1016/j.earscirev.2019.102936.
603 Holland, T. J. B., and Powell, R. (2011). An improved and extended internally consistent
604 thermodynamic dataset for phases of petrological interest, involving a new equation
605 of state for solids. Journal of Metamorphic Geology, 29, 333-383.
606 Hwang, S.L., Shen, P.Y., Chu, H.T., Yui, T.F., Liou, J.G., and Sobolev, N.V. (2009)
607 Kumdykolite, an orthorhombic polymorph of albite, from the Kokchetav
608 ultrahigh-pressure massif, Kazakhstan. European Journal of Mineralogy, 21(6),
609 1325-1334.
610 Kanzaki, M., Xue, X., Amalberti, J., and Zhang, Q. (2012) Raman and NMR

611 spectroscopic characterization of high-pressure K-cymrite ($KAlSi_3O_8 \cdot H_2O$) and its
612 anhydrous form (kokchetavite). Journal of Mineralogical and Petrological Sciences,
613 107(2), 114-119.
614 Kerrick, D., and Connolly, J. (2001) Metamorphic devolatilization of subducted marine
615 sediments and the transport of volatiles into the Earth's mantle. Nature, 411,
616 293-296.
617 Lafuente, B., Downs, R.T., Yang, H., Stone, N. (2015) The power of databases: the
618 RRUFF project, In: Highlights in Mineralogical Crystallography, T. Armbruster and
619 R.M. Danisi, eds., Belin, Germany, W. De Gruter, pp. 1-30.
620 Li, W.C., Chen, R.X., Zheng, Y.F., Tang, H., and Hu, Z. (2016) Two episodes of partial
621 melting in ultrahigh-pressure migmatites from deeply subducted continental crust in
622 the Sulu orogen, China. Geological Society of America Bulletin, 128(9-10),
623 1521-1542.
624 Liu, F.L, Robinson, P.T., Gerdes, A., Xue, H., Liu, P., and Liou, J.G. (2010) Zircon U-Pb
625 ages, REE concentrations and Hf isotope compositions of granitic leucosome and
626 pegmatite from the north Sulu UHP terrane in China: Constraints on the timing and
627 nature of partial melting. Lithos, 117(1-4), 247-268.
628 McConnell, J. (1960) Vaterite from Ballycraigy, Larne, Northern Ireland. Mineralogical
629 Magazine and Journal of the Mineralogical Society, 32(250), 535-544.
630 https://doi.org/10.1180/minmag.1960.032.250.03.
631 Nakamura, D., and Hirajima, T. (2000) Granulite-facies overprinting of

632 ultrahigh-pressure metamorphic rocks, northeastern Su-Lu region, eastern China.
633 Journal of Petrology, 41(4), 563-582.
634 Namba, Y., Heidarpour, E., and Nakayama, M. (1992) Size effects appearing in the
635 Raman spectra of polycrystalline diamonds. Journal of Applied Physics, 72(5),
636 1748-1751.
637 Nasdala, L., Steger, S., and Reissner, C. (2016) Raman study of diamond-based abrasives,
638 and possible artefacts in detecting UHP microdiamond. Lithos, 265, 317-327.
639 Ogino, T., Suzuki, T., and Sawada, K. (1987) The formation and transformation
640 mechanism of calcium carbonate in water. Geochimica et Cosmochimica Acta,
641 51(10), 2757-2767.
642 Pistorius, C.W. (1963) Thermal decomposition of portlandite and xonotlite to high
643 pressures and temperatures. American Journal of Science, 261(1), 79-87.
644 Putnis, A., Prieto, M., and Fernandez-Diaz, L. (1995) Fluid supersaturation and
645 crystallization in porous media. Geological Magazine, 132(1), 1-13.
646 Rahl, J., Anderson, K., Brandon, M., and Fassoulas, C. (2005) Raman spectroscopic
647 carbonaceous material thermometry of low-grade metamorphic rocks: Calibration
648 and application to tectonic exhumation in Crete, Greece. Earth and Planetary
649 Science Letters, 240(2), 339-354.
650 Rodgers, A.L. (1983) Common ultrastructural features in human calculi. Micron and
651 Microscopica Acta, 14(3), 219-224.
652 Rodriguez-Blanco, J.D., Shaw, S., and Benning, L.G. (2011) The kinetics and

653 mechanisms of amorphous calcium carbonate (ACC) crystallization to calcite, via
654 vaterite. Nanoscale, 3(1), 265-271.
655 Rosenberg, C.L., and Handy, M.R. (2005) Experimental deformation of partially melted
656 granite revisited: implications for the continental crust. Journal of Metamorphic
657 Geology, 23(1), 19-28.
658 Rosso, K. M., and Bodnar, R. J. (1995) Microthermometric and Raman spectroscopic
659 detection limits of CO_2 in fluid inclusions and the Raman spectroscopic
660 characterization of CO_2. Geochimica et Cosmochimica Acta, 59(19), 3961-3975.
661 Schopf, J.W., Kudryavtsev, A.B., Agresti, D.G., Czaja, A.D., and Wdowiak, T.J. (2005)
662 Raman imagery: A new approach to assess the geochemical maturity and biogenicity
663 of permineralized Precambrian fossils. Astrobiology, 5(3), 333-371.
664 Shmulovich, K., Graham, C., and Yardley, B. (2001) Quartz, albite and diopside
665 solubilities in H_2O-NaCl and H_2O-CO_2 fluids at 0.5-0.9 GPa. Contributions to
666 Mineralogy and Petrology, 141(1), 95-108.
667 Stöckhert, B., Trepmann, C.A., and Massonne, H.J. (2009) Decrepitated UHP fluid
668 inclusions: about diverse phase assemblages and extreme decompression rates
669 (Erzgebirge, Germany). Journal of Metamorphic Geology, 27(9), 673-684.
670 Sverjensky, D.A., and Huang, F. (2015) Diamond formation due to a pH drop during
671 fluid-rock interactions. Nature Communications, 6, 8702.
672 Sverjensky, D.A., Stagno, V., and Huang, F. (2014) Important role for organic carbon in
673 subduction-zone fluids in the deep carbon cycle. Nature Geoscience, 7(12), 909-913.

674 Turnbull, A.G. (1973) A thermochemical study of vaterite. Geochimica et Cosmochimica
675 Acta, 37(6), 1593-1601.
676 Váczi, T. (2014) A new, simple approximation for the deconvolution of instrumental
677 broadening in spectroscopic band profiles. Applied Spectroscopy, 68(11),
678 1274-1278.
679 Veinott, G.I., Porter, T.R., and Nasdala, L. (2009) Using Mg as a proxy for crystal
680 structure and Sr as an indicator of marine growth in vaterite and aragonite otoliths of
681 aquaculture rainbow trout. Transactions of the American Fisheries Society, 138,
682 1157-1165.
683 Vogel, W. (1977) Phase separation in glass. Journal of Non-Crystalline Solids, 25(1-3),
684 170-214.
685 Wallis, S., Tsuboi, M., Suzuki, K., Fanning, M., Jiang, L., and Tanaka, T. (2005) Role of
686 partial melting in the evolution of the Sulu (eastern China) ultrahigh-pressure terrane.
687 Geology, 33(2), 129-132.
688 Wang, Q., Ishiwatari, A., Zhao, Z., Hirajima, T., Hiramatsu, N., Enami, M., Zhai, M., and
689 Cong, B. (1993) Coesite-bearing granulite retrograded from eclogite in Weihai,
690 eastern China. European Journal of Mineralogy, 5, 141-152.
691 Wehrmeister, U., Soldati, A.L., Jacob, D.E., Häger, T., and Hofmeister, W. (2009) Raman
692 spectroscopy of synthetic, geological and biological vaterite: a Raman spectroscopic
693 study. Journal of Raman Spectroscopy, 41, 193-201.
694 Xu, H., Ye, K., Song, Y., Chen, Y., Zhang, J., Liu, Q., and Guo, S. (2013) Prograde

metamorphism, decompressional partial melting and subsequent melt fractional crystallization in the Weihai migmatitic gneisses, Sulu UHP terrane, eastern China. Chemical Geology, 341, 16-37.

Zhang, R., Liou, J., and Ernst, W. (1995) Ultrahigh-pressure metamorphism and decompressional *P-T* paths of eclogites and country rocks from Weihai, eastern China. Island Arc, 4(4), 293-309.

Zotov, N., and Keppler, H. (2002) Silica speciation in aqueous fluids at high pressures and high temperatures. Chemical Geology, 184(1-2), 71-82.

FIGURE 1. (**a**) Simplified geological map of the Weihai region, north Sulu UHP metamorphic terrane (modified after Liu et al., 2010). (**b**) outcrop photograph showing the migmatite studied. (**c**) mineral assemblages in leucosome and mesosome. plane-polarized light. Abbreviations: Amp = amphibole; Bt = biotite; Kfs = K-feldspar; Pl = plagioclase; Qz = quartz.

FIGURE 2. Photomicrographs showing zircon texture and inclusions. (**a**) CL image. (**b**) reflected light photomicrograph. (**c** and **d**) transmitted light photomicrographs. (**e-l**) Raman maps of the inclusions. -2.4 μm in (**e**) indicates the mapped section at the depth of 2.4 μm beneath the polishing surface. CM-bearing inclusions: 4, 5 and 9; CO_2 fluid inclusions: 11 and 12; Melt inclusions: 2, 6, 8, 13 and 14; Oxide and sulphate solid inclusions: 1, 3, 7 (Rt + Hem) and 10. Abbreviations: Ab = albite; Anh = anhydrite; Ant = anatase; Arg = aragonite; Brt = barite; Cal = calcite; CM = carbonaceous material; Dia =

716 diamond; Hem = hematite; Kok = kokchetavite; Kml = kumdykolite; Ms = muscovite; Rt
717 = rutile; Vtr = vaterite; Zrn = zircon.

718 **FIGURE 3.** Representative Raman spectra of materials in the inclusions. The Raman
719 bands of zircon are marked with star (1007, 976, 439, 357, 233, 224 and 201 cm^{-1}).

720 **FIGURE 4.** SE and BF images obtained from inclusion 4. (**a**) SE image of air-view
721 showing FIB-milled trench and inclusion in vertical cross-section S2. (**b**) SE image of
722 vertical cross-section S8. (**c**) BF image of vertical cross-section S10. C-Si-O: consisting
723 of C, Si and O; Zr-Si-O: consisting of Zr, Si and O. (**d-h**) X-ray compositional maps of
724 vertical cross-section S10.

725 **FIGURE 5.** SE images and X-ray compositional maps obtained from inclusion 5. (**a**) SE
726 image of air-view showing FIB-milled trenches and inclusion in vertical cross-section S5.
727 (**b** and **c**) SE images of vertical cross-sections S6 and S9 at different stages of FIB milling
728 process. (**d-h**) X-ray compositional maps of vertical cross-section S9. The mapping area
729 is marked with yellow rectangle in image (**c**).

730 **FIGURE 6.** SE and Raman images obtained from the foil of inclusion 5. (**a**) SE image.
731 (**b**) Raman map. (**c**) Raman spectrum of diamond at the position with plus mark in (**b**). (**d**)
732 Band position and FWHM of diamond before and after FIB milling. (**e**) Raman spectra of
733 highly disordered CM. Band fitting for highly disordered CM is also shown (see the text
734 in "Discussion").

735 **FIGURE 7.** TEM images obtained from inclusion 4. (**a**) BF image showing the materials.
736 C-Si-O and Zr-Si-O are amorphous materials. (**b** and **c**) BF images showing nanometer

diamonds in the amorphous materials. (**d** and **e**) HRTEM images showing a nanometer diamond enclosed in amorphous C-Si-O material. The diamond displays one set of lattice fringes and fully coupled and welded interface with the C-Si-O material.

FIGURE 8. Representative X-ray compositional spectra and SAED patterns of the materials in inclusion 4. (**a** and **b**) vaterite. (**c**) aragonite. (**d**-**f**) micrometer diamonds. (**g**-**i**) nanometer diamonds; (**j** and **l**) amorphous C-Si-O material. (**k** and **m**) amorphous Zr-Si-O material. Cu, Ga and Cr are from contamination. Cu is from supportive copper grid, Ga from FIB milling and Cr from TEM sample holder.

FIGURE 9. Compositional plots of the C-Si-O and Zr-Si-O materials in the Zr-C-Si triangle.

FIGURE 10. TEM observations obtained from inclusion 5. (**a**) BF image. nc-Zr-Si-O: nanocrystals plus amorphous material; a-Zr-Si-O: amorphous Zr-Si-O material. (**b**) X-ray compositional map showing Zr zoning in the banded Zr-Si-O material. (**c** and **d**) micrometer diamonds. (**e** and **f**) nc-Zr-Si-O material. (**g** and **h**) a-Zr-Si-O material. (**i** and **j**) C-Si-O material.

FIGURE 11. Exhumation *P*-*T* path of the rocks in the Weihai region and sketch *P*-*T* evolutions of inclusions 4 and 5. The *P*-*T* estimates of the rocks (red circles with errors) are from Zhang et al. (1995) and Nakamura and Hirajima (2000). The stability fields for vesuvianite with *P4/nnc* polytype and xonotlite are from Gnos and Armnruster (2006) and Pistorious (1963), respectively. Diamond–graphite and coesite–quartz equilibrium curves are calculated using Thermocalc (Holland and Powell 2011).

This is the peer-reviewed, final accepted version for American Mineralogist, published by the Mineralogical Society of America.
The published version is subject to change. Cite as Authors (Year) Title. American Mineralogist, in press.
DOI: https://doi.org/10.2138/am-2021-7940. http://www.minsocam.org/

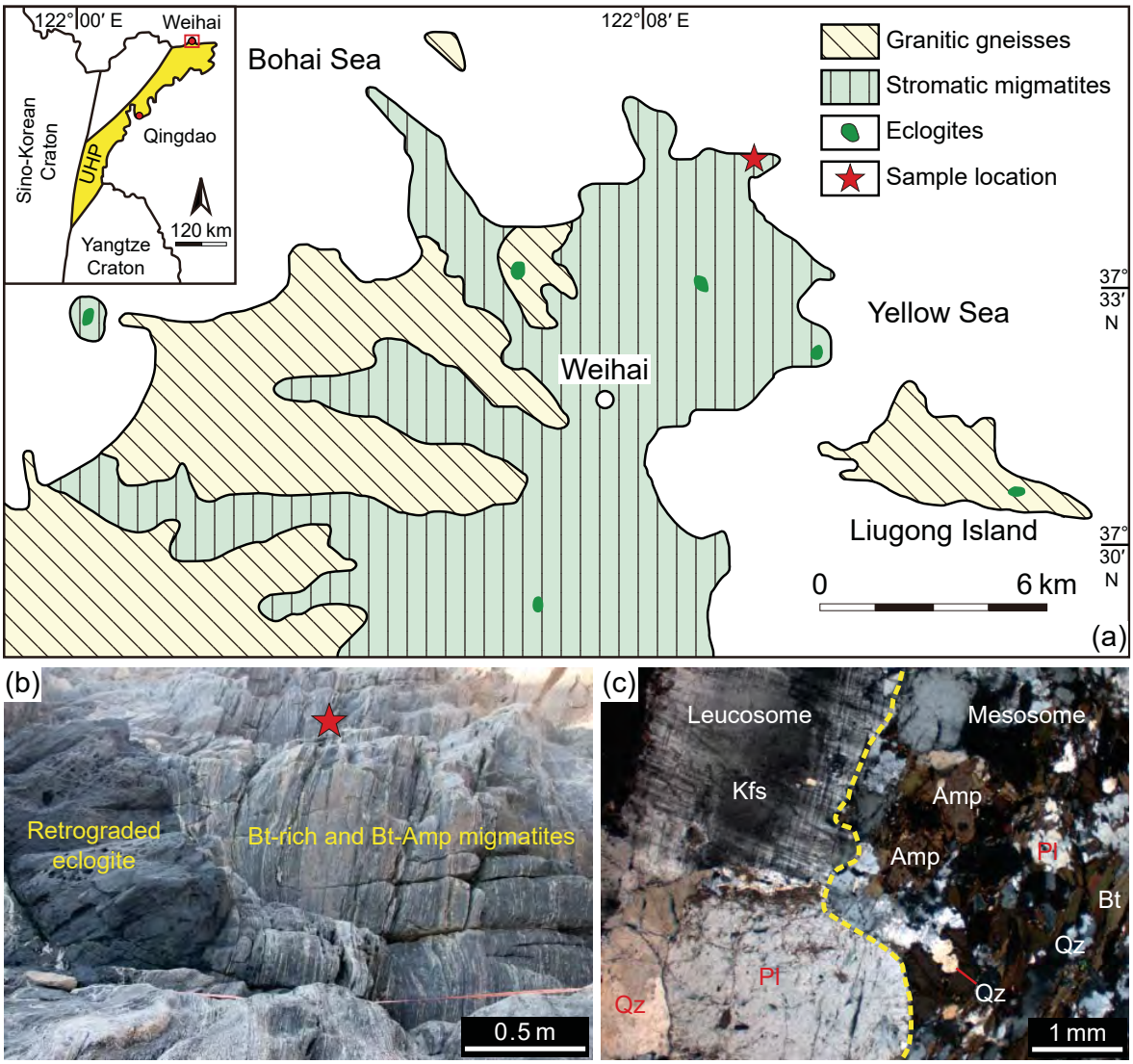

Fig. 1

This is the peer-reviewed, final accepted version for American Mineralogist, published by the Mineralogical Society of America.
The published version is subject to change. Cite as Authors (Year) Title. American Mineralogist, in press.
DOI: https://doi.org/10.2138/am-2021-7940. http://www.minsocam.org/

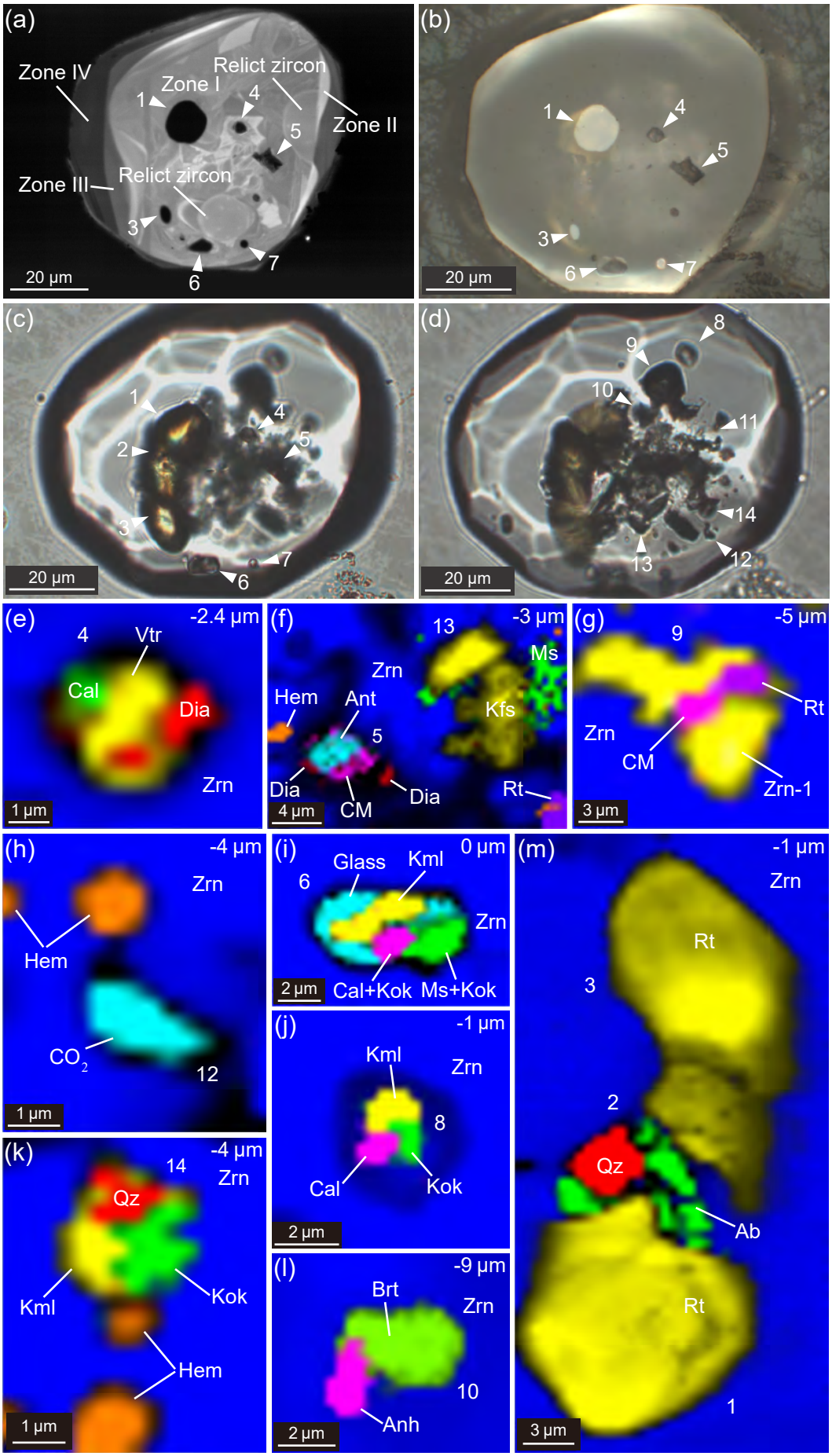

Fig. 2

This is the peer-reviewed, final accepted version for American Mineralogist, published by the Mineralogical Society of America.
The published version is subject to change. Cite as Authors (Year) Title. American Mineralogist, in press.
DOI: https://doi.org/10.2138/am-2021-7940. http://www.minsocam.org/

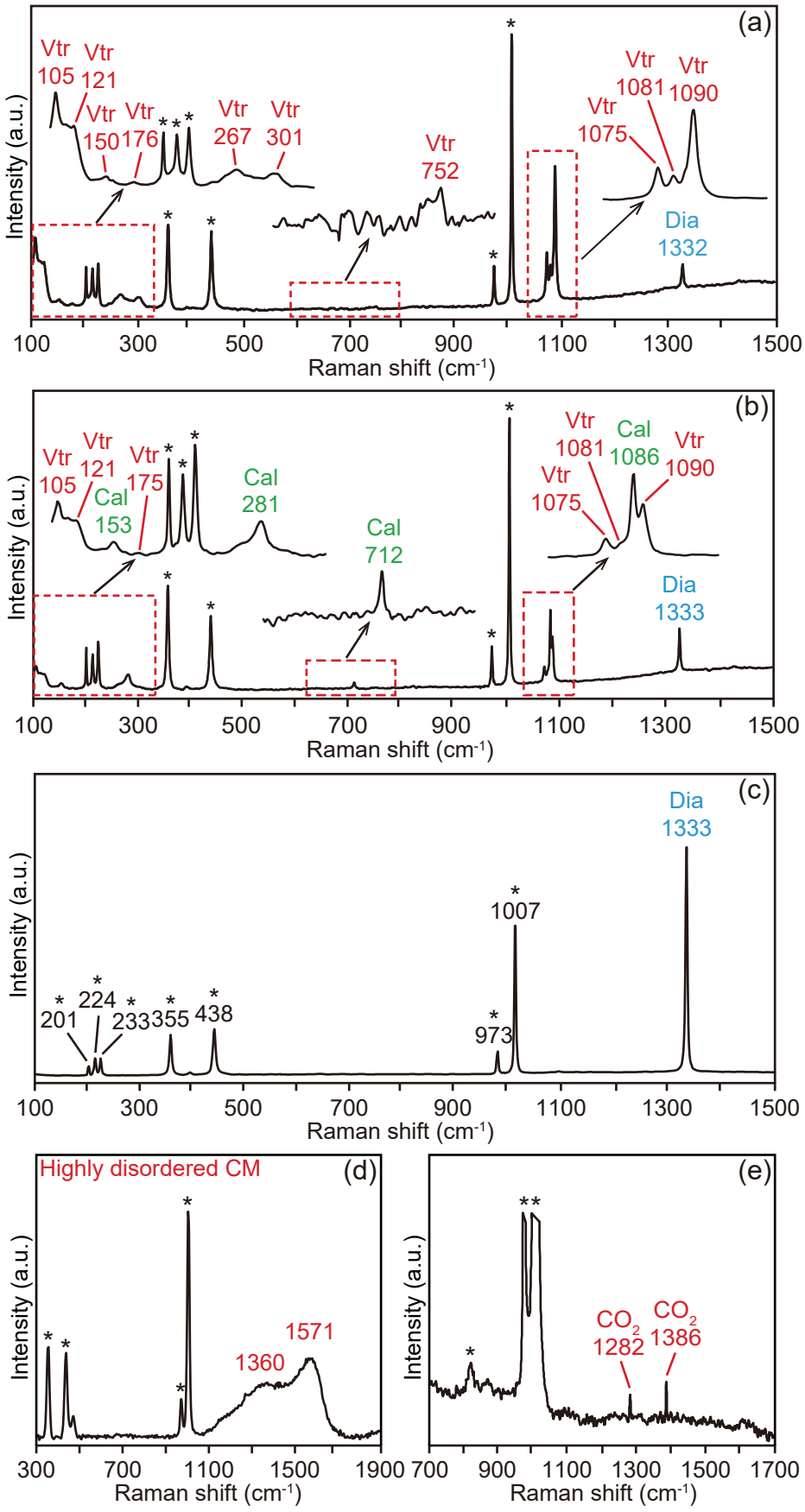

Fig. 3

This is the peer-reviewed, final accepted version for American Mineralogist, published by the Mineralogical Society of America.
The published version is subject to change. Cite as Authors (Year) Title. American Mineralogist, in press.
DOI: https://doi.org/10.2138/am-2021-7940. http://www.minsocam.org/

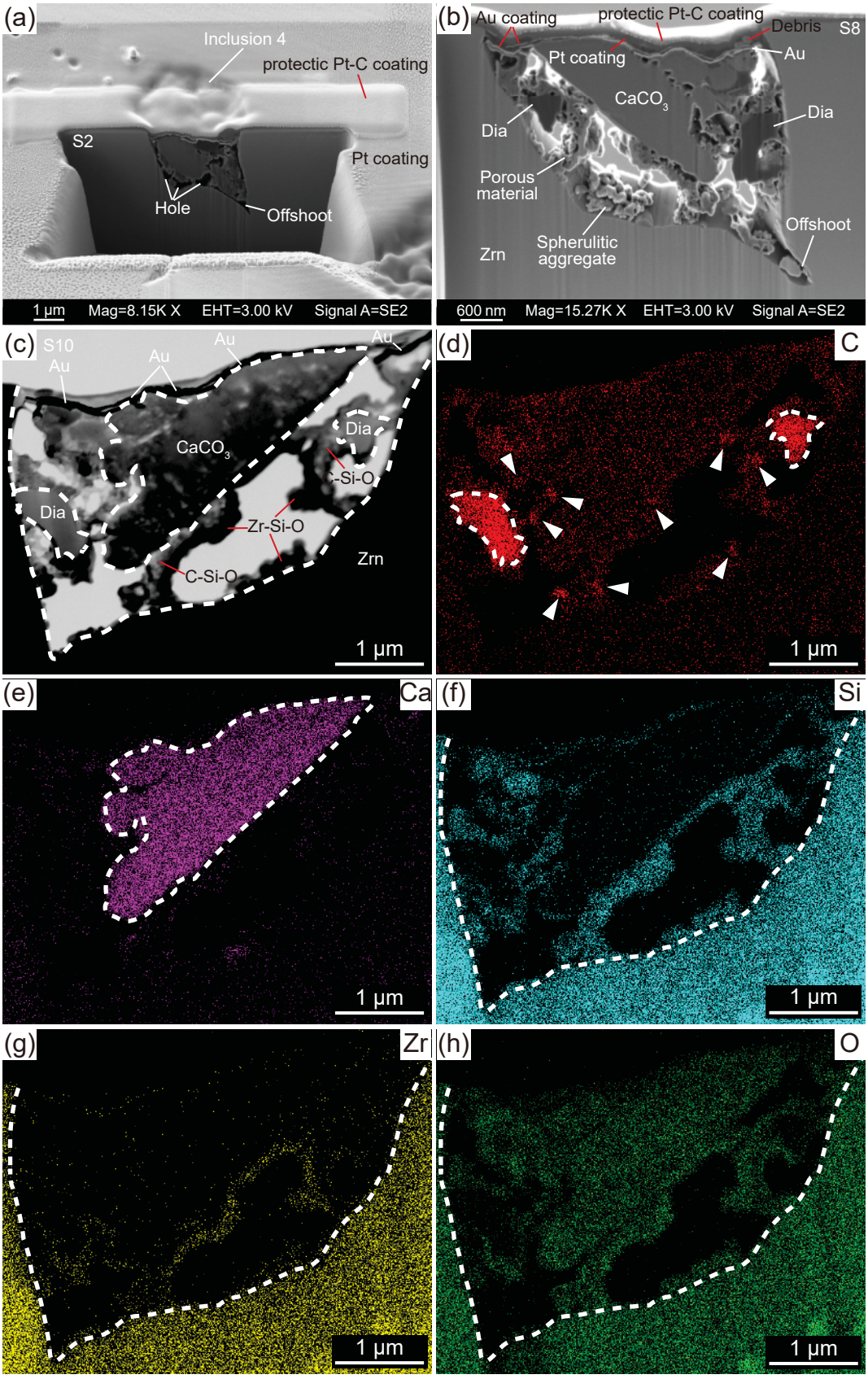

Fig. 4

This is the peer-reviewed, final accepted version for American Mineralogist, published by the Mineralogical Society of America.
The published version is subject to change. Cite as Authors (Year) Title. American Mineralogist, in press.
DOI: https://doi.org/10.2138/am-2021-7940. http://www.minsocam.org/

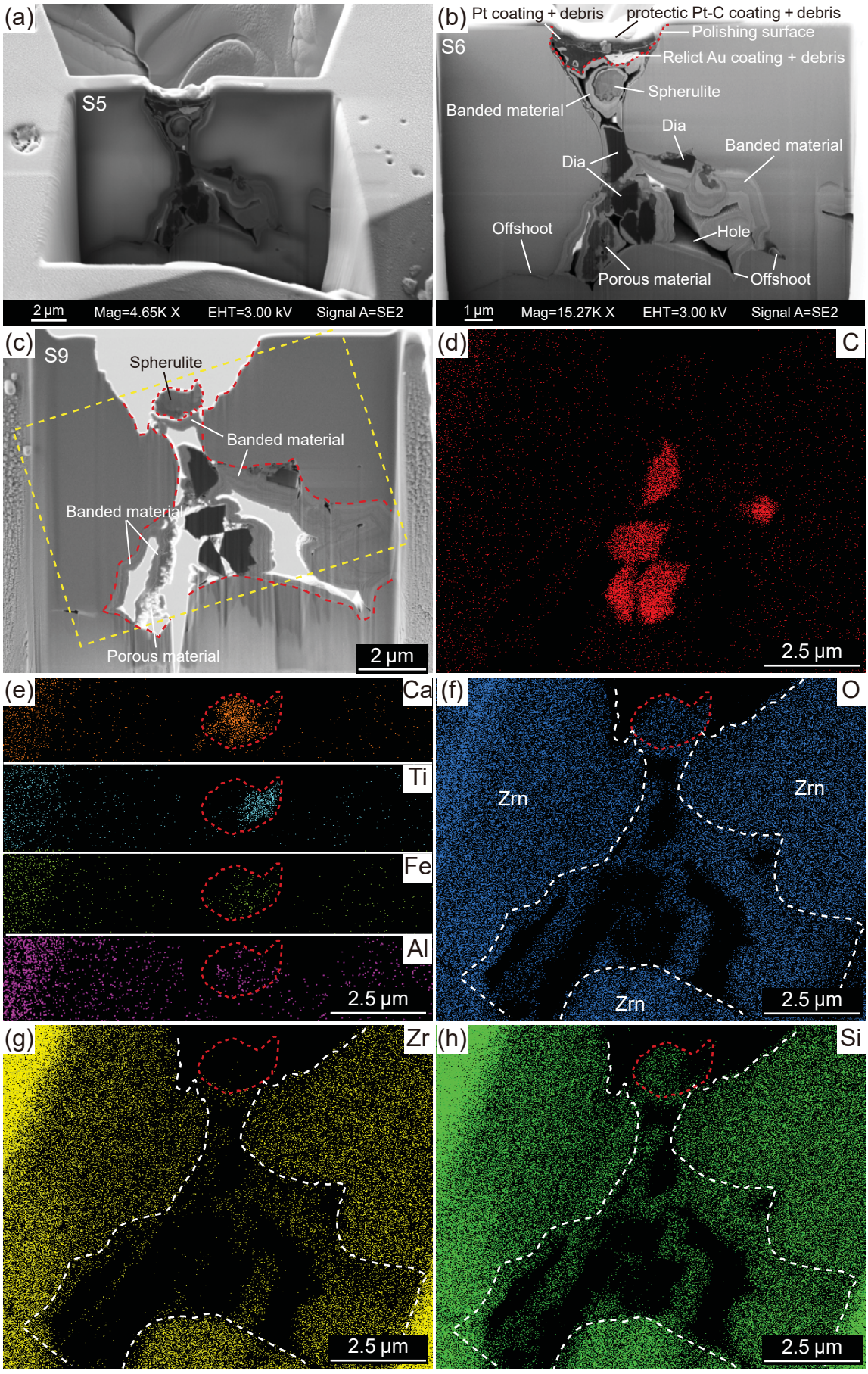

Fig. 5

This is the peer-reviewed, final accepted version for American Mineralogist, published by the Mineralogical Society of America.
The published version is subject to change. Cite as Authors (Year) Title. American Mineralogist, in press.
DOI: https://doi.org/10.2138/am-2021-7940. http://www.minsocam.org/

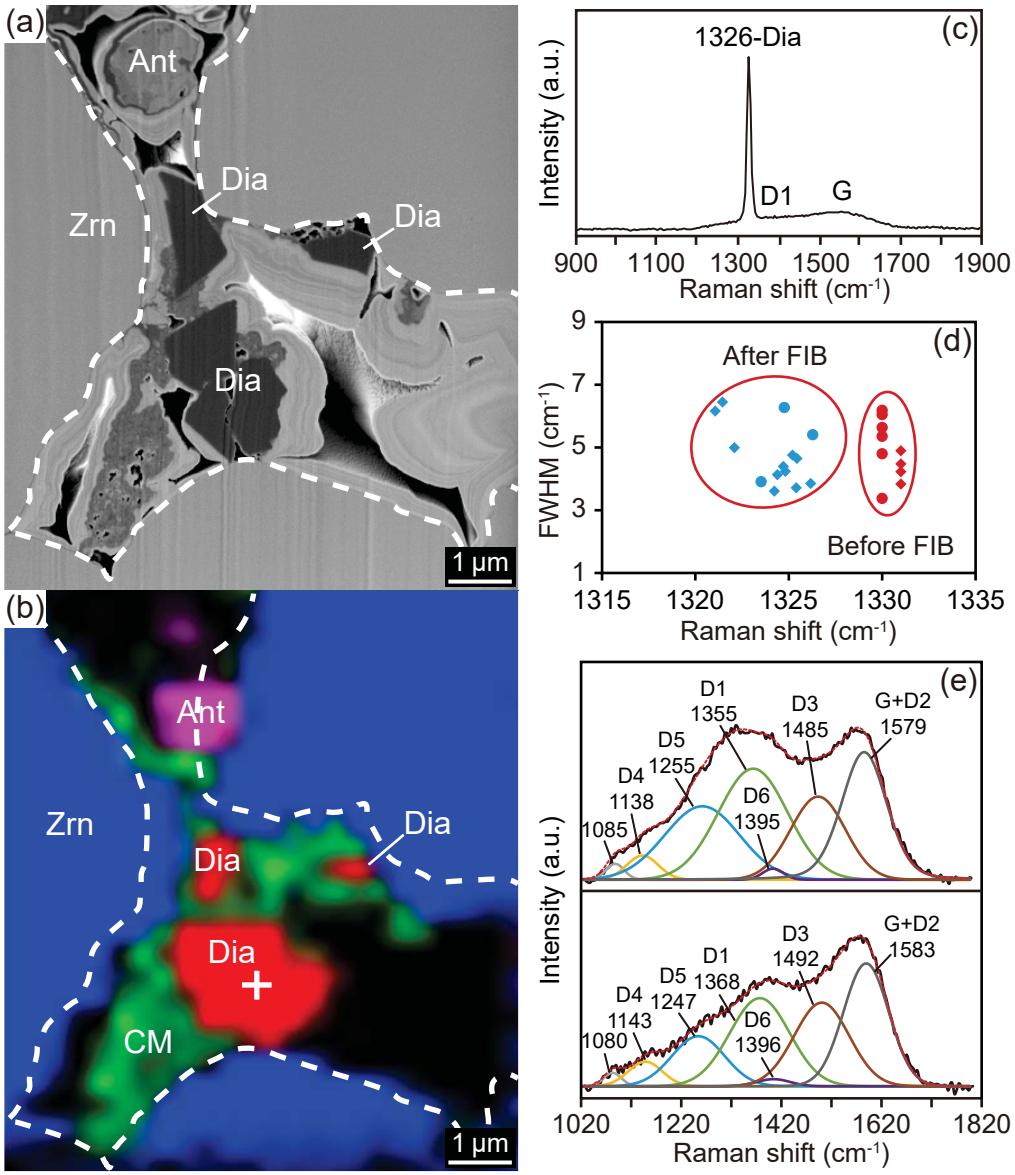

Fig. 6

This is the peer-reviewed, final accepted version for American Mineralogist, published by the Mineralogical Society of America.
The published version is subject to change. Cite as Authors (Year) Title. American Mineralogist, in press.
DOI: https://doi.org/10.2138/am-2021-7940. http://www.minsocam.org/

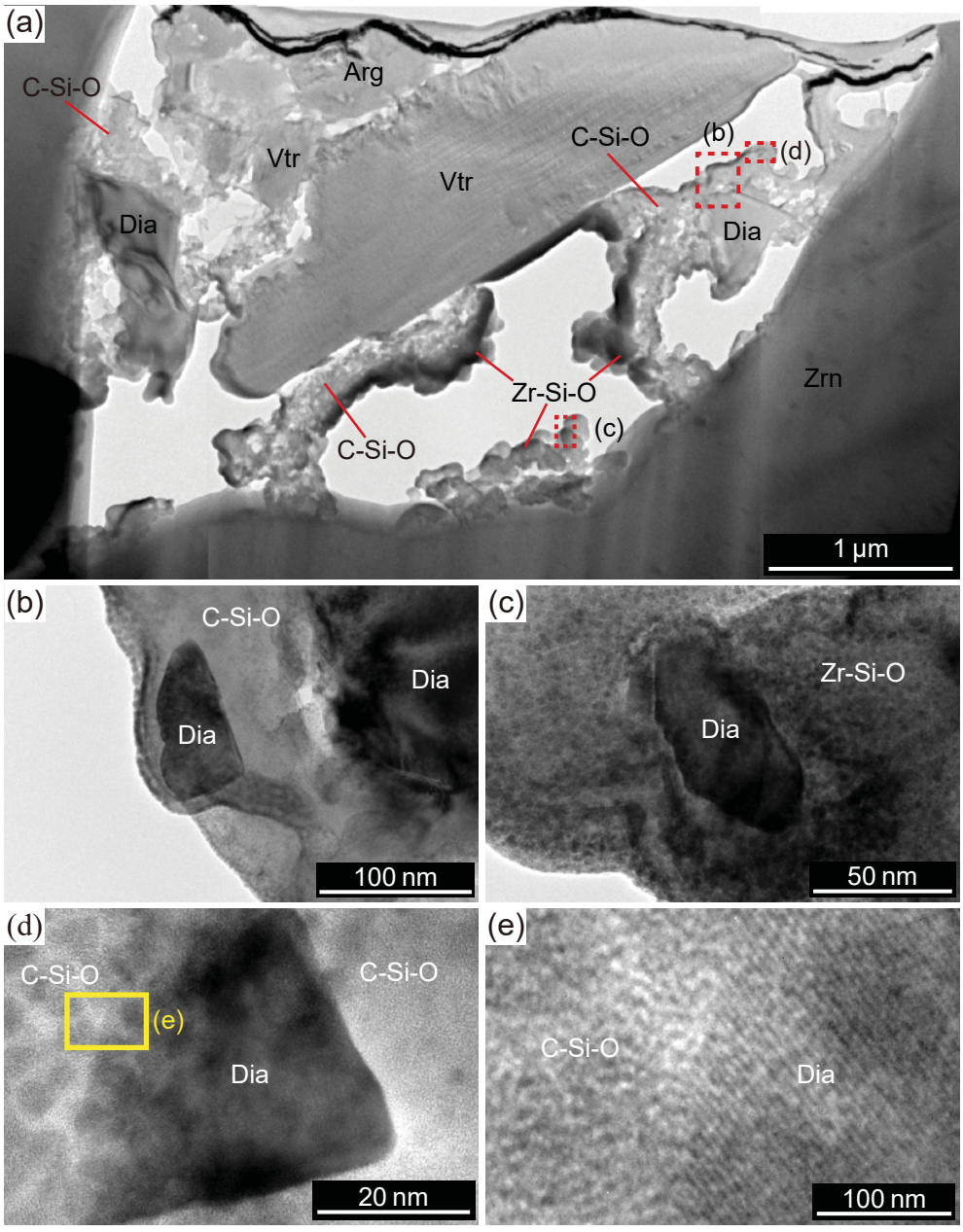

Fig. 7

This is the peer-reviewed, final accepted version for American Mineralogist, published by the Mineralogical Society of America.
The published version is subject to change. Cite as Authors (Year) Title. American Mineralogist, in press.
DOI: https://doi.org/10.2138/am-2021-7940. http://www.minsocam.org/

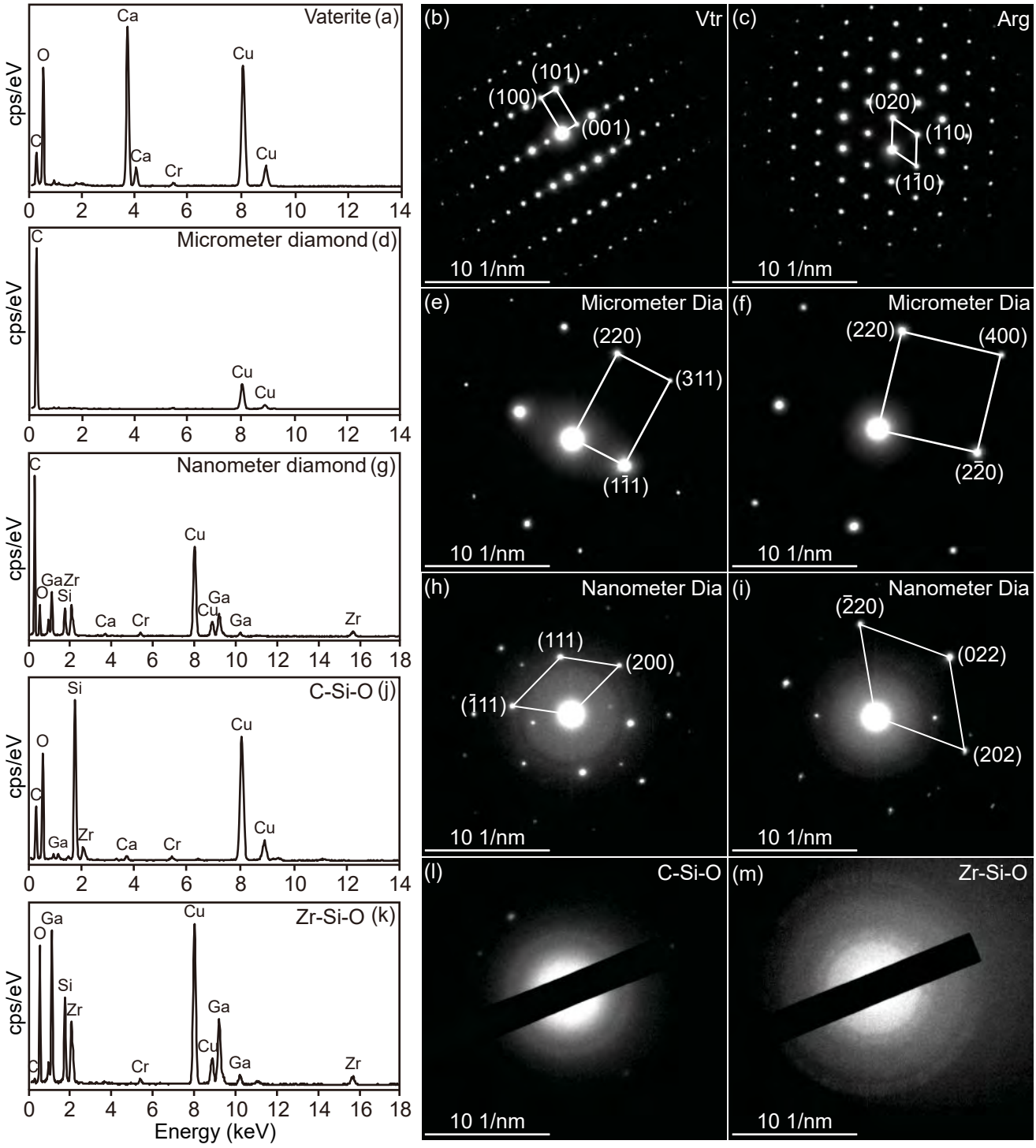

Fig. 8

This is the peer-reviewed, final accepted version for American Mineralogist, published by the Mineralogical Society of America.
The published version is subject to change. Cite as Authors (Year) Title. American Mineralogist, in press.
DOI: https://doi.org/10.2138/am-2021-7940. http://www.minsocam.org/

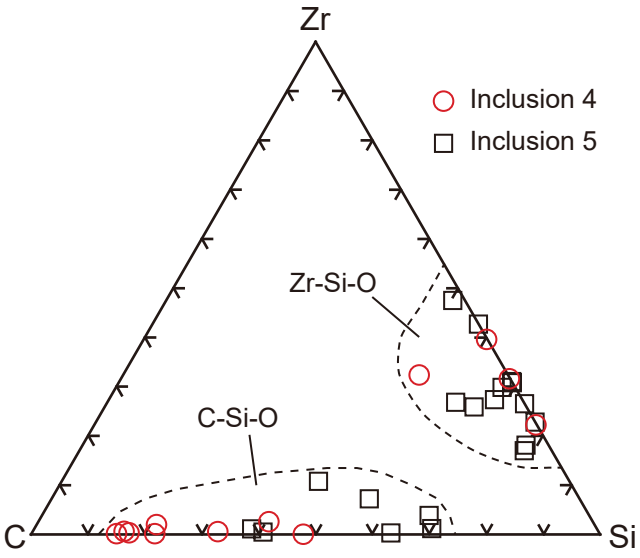

Fig. 9

This is the peer-reviewed, final accepted version for American Mineralogist, published by the Mineralogical Society of America.
The published version is subject to change. Cite as Authors (Year) Title. American Mineralogist, in press.
DOI: https://doi.org/10.2138/am-2021-7940. http://www.minsocam.org/

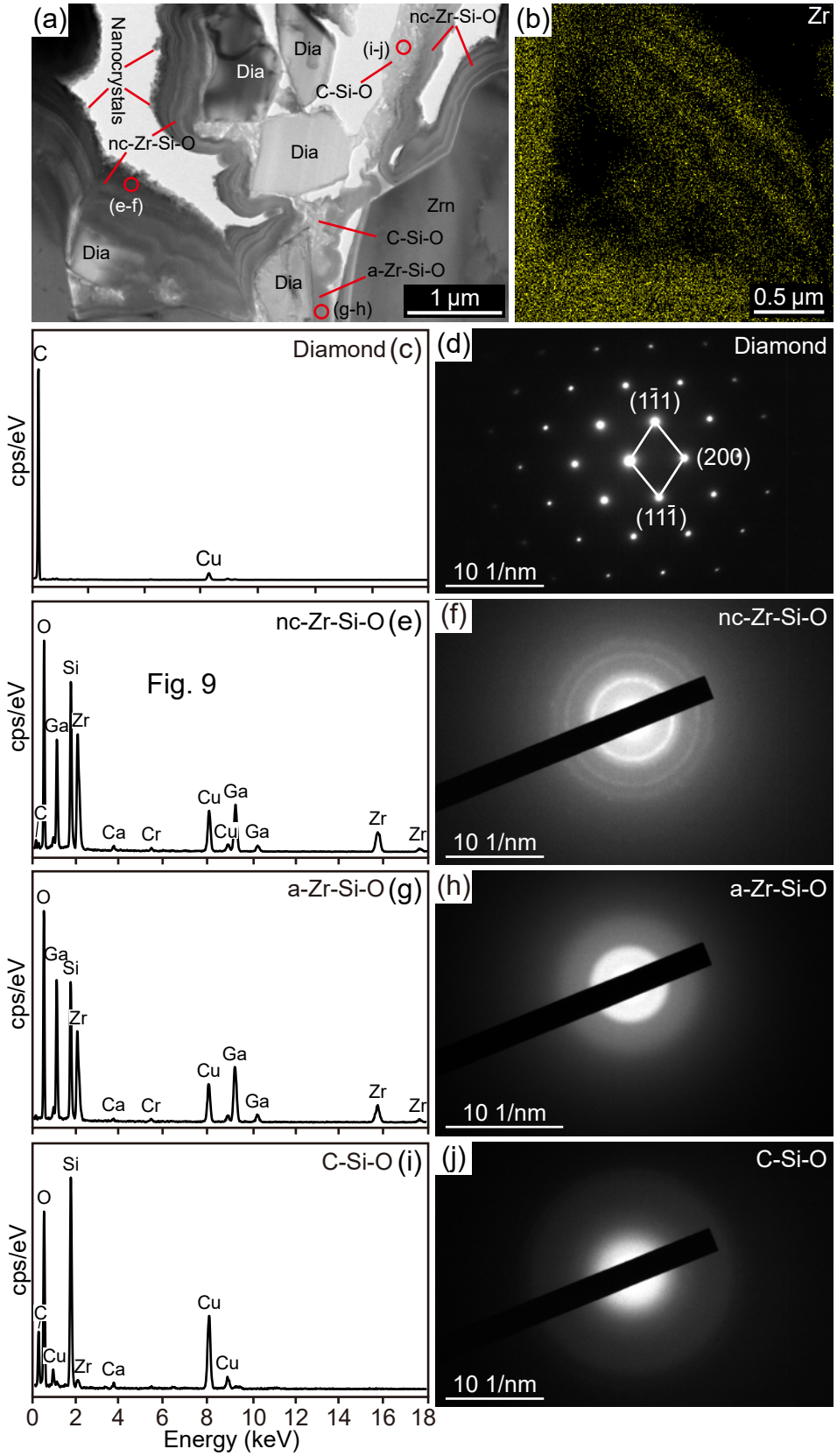

Fig. 9

Fig. 10

This is the peer-reviewed, final accepted version for American Mineralogist, published by the Mineralogical Society of America.
The published version is subject to change. Cite as Authors (Year) Title. American Mineralogist, in press.
DOI: https://doi.org/10.2138/am-2021-7940. http://www.minsocam.org/

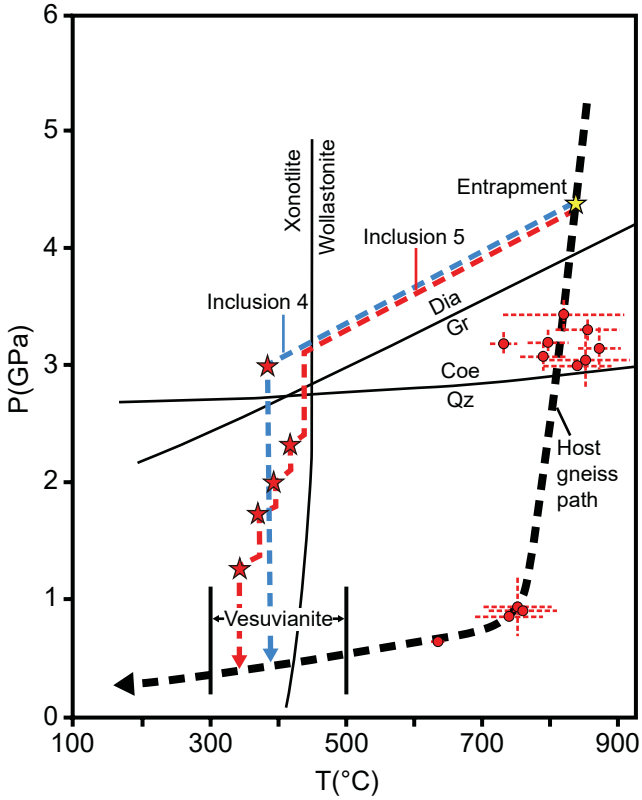

Fig. 11